AGU PUBLICATIONS

Water Resources Research

RESEARCH ARTICLE
10.1002/2016WR019749

Key Points:
- We present a set of meter-scale sandbox experiments designed to replicate field-scale CO_2 injection configuration and contrast in fluid properties
- Multiple drainage/imbibition events are used to achieve larger plume footprints, higher trapping efficiency, and larger total mass trapped
- X-ray attenuation is used for accurate quantification of CO_2-analog saturation and mass balance calculations

Supporting Information:
- Figure S1
- Data Set S1
- Data Set S2
- Data Set S3

Correspondence to:
L. Trevisan,
luca.trevisan@gmail.com

Citation:
Trevisan, L., R. Pini, A. Cihan, J. T. Birkholzer, Q. Zhou, A. González-Nicolás, and T. H. Illangasekare (2017), Imaging and quantification of spreading and trapping of carbon dioxide in saline aquifers using meter-scale laboratory experiments, *Water Resour. Res.*, *53*, doi:10.1002/2016WR019749.

Received 2 SEP 2016
Accepted 19 DEC 2016
Accepted article online 27 DEC 2016

Imaging and quantification of spreading and trapping of carbon dioxide in saline aquifers using meter-scale laboratory experiments

Luca Trevisan[1,2], Ronny Pini[3,4], Abdullah Cihan[5], Jens T. Birkholzer[5], Quanlin Zhou[5], Ana González-Nicolás[1,5], and Tissa H. Illangasekare[1]

[1]Center for Experimental Study of Subsurface Environmental Processes, Department of Civil and Environmental Engineering, Colorado School of Mines, Golden, Colorado, USA, [2]Now at Gulf Coast Carbon Center, Bureau of Economic Geology, Jackson School of Geosciences, University of Texas at Austin, Austin, Texas, USA, [3]Department of Petroleum Engineering, Colorado School of Mines, Golden, Colorado, USA, [4]Now at Department of Chemical Engineering, Imperial College, London, UK, [5]Energy Geosciences Division, Lawrence Berkeley National Laboratory, University of California, Berkeley, California, USA

Abstract The role of capillary forces during buoyant migration of CO_2 is critical toward plume immobilization within the postinjection phase of a geological carbon sequestration operation. However, the inherent heterogeneity of the subsurface makes it very challenging to evaluate the effects of capillary forces on the storage capacity of these formations and to assess in situ plume evolution. To overcome the lack of accurate and continuous observations at the field scale and to mimic vertical migration and entrapment of realistic CO_2 plumes in the presence of a background hydraulic gradient, we conducted two unique long-term experiments in a 2.44 m $\times$ 0.5 m tank. X-ray attenuation allowed measuring the evolution of a CO_2-surrogate fluid saturation, thus providing direct insight into capillarity-dominated and buoyancy-dominated flow processes occurring under successive drainage and imbibition conditions. The comparison of saturation distributions between two experimental campaigns suggests that layered-type heterogeneity plays an important role on nonwetting phase (NWP) migration and trapping, because it leads to (i) longer displacement times (3.6 months versus 24 days) to reach stable trapping conditions, (ii) limited vertical migration of the plume (with center of mass at 39% versus 55% of aquifer thickness), and (iii) immobilization of a larger fraction of injected NWP mass (67.2% versus 51.5% of injected volume) as compared to the homogenous scenario. While these observations confirm once more the role of geological heterogeneity in controlling buoyant flows in the subsurface, they also highlight the importance of characterizing it at scales that are below seismic resolution (1–10 m).

1. Introduction

Geological carbon storage (GCS) has the potential to stabilize and eventually reduce anthropogenic emissions of CO_2 to the atmosphere, thus facilitating the transition from fossil energy production to an extensive use of renewables. For GCS to considerably reduce global carbon emissions, large volumes of CO_2 have to be stored underground. This can be accomplished by taking advantage of the heterogeneous nature of deep brine-bearing sedimentary formations and by designing appropriate injection schemes. The heterogeneous nature of geological media plays a critical role in controlling the migration and entrapment of injected CO_2 by affecting the efficiency of both dissolution [*Agartan et al.*, 2015; *Farajzadeh et al.*, 2011] and capillary trapping [*Bryant et al.*, 2008; *Trevisan et al.*, 2015]. Hence, it becomes crucial to consider the influence of natural heterogeneity on storage capacity and efficiency whenever candidate reservoirs are identified [*Kopp et al.*, 2009]. Assuming that most candidate reservoirs are inherently heterogeneous, we can expect a persistent presence of so-called capillary barriers that possess variable spatial continuity and that lead to the plume concentrating in high-permeability streaks and pooling behind less permeable layers. Because characterizing deep reservoirs' heterogeneity and assessing in situ plume behavior (by means of, e.g., preferential flow and fluid saturation evolution) is practically difficult, intermediate scale (dm-m) immiscible displacement experiments represent a convenient method for studying the influence of heterogeneity

on macroscale migration and trapping phenomena. A further advantage of synthetic aquifers is the ability to test injection schemes that have potential applications in real storage scenarios. In the context of this work, we investigate the role of capillary forces during buoyant migration of CO_2 as a critical factor toward plume immobilization during postinjection of carbon storage in deep saline aquifers.

In general, the action of capillarity on immiscible fluid displacement manifests itself via two major phenomena, namely hysteresis and capillary barrier, causing occurrence of nonwetting phase (NWP) at different saturations across the porous medium. The importance of these phenomena has been pointed out by several numerical modeling studies focusing on a variety of specific aspects at the field scale [*Bryant et al*., 2008; *Deng et al*., 2012; *Doughty and Pruess*, 2004; *Flett et al*., 2007; *Saadatpoor et al*., 2010] and at the sub-meter scale [*Kuo and Benson*, 2015; *Li and Benson*, 2015; *Ritzi et al*., 2016; *Trevisan et al*., 2017]. For example, spatial correlation of the permeability (k) field as well as interconnectivity of high-k preferential flow pathways have a critical impact on CO_2 migration and trapping in saline aquifers [*Gershenzon et al*., 2015; *Han et al*., 2010; *Ide et al*., 2007; *Lengler et al*., 2010; *Tian et al*., 2016]. The modeling approach has also been followed, either numerically [*Buscheck et al*., 2012; *Gasda et al*., 2008; *Goater et al*., 2013; *Yamamoto et al*., 2009] or analytically [*Gunn and Woods*, 2011; *Hesse et al*., 2006; *MacMinn et al*., 2010; *Zimoch et al*., 2011], to understand the behavior of a CO_2 plume in concomitance with regional groundwater flow and sloping caprock. Injection strategies aimed at enhancing the storage capacity and efficiency of saline formations have also been explored by means of numerical models [*Buscheck et al*., 2012; *Cameron and Durlofsky*, 2012; *Shamshiri and Jafarpour*, 2012; *Cihan et al*., 2015; *González-Nicolás et al*., 2016*; Huber et al*., 2016; *Rasmusson et al*., 2016].

While numerical simulations have shed light on the influence of some of the geological and engineering aspects that control CO_2 trapping mechanisms, validation by means of experiments is still lacking. Hereby, the difficulty in carrying out controlled field experiments has always involved uncertainty related to the rigorous application of boundary conditions and the exact distribution of sandstone rock types. Most of the work to date has focused on nonaqueous phase liquid (NAPL) migration observed in sandbox experiments [e.g., *Barth et al*., 2003; *Fagerlund et al*., 2007; *Glass et al*., 2000; *Kueper and Frind*, 1991], while studies that specifically address GCS are quite scarce and are limited to cm-to-m observations of immiscible [*Pini et al*., 2012; *Polak et al*., 2015; *Trevisan et al*., 2014; *Werner et al*., 2014; *Zhao et al*., 2014] and miscible displacements [*Agartan et al*., 2015; *Neufeld et al*., 2010]. A dimensional analysis approach has also been proposed to reconcile laboratory scales and field scales [*Cinar et al*., 2009; *Polak et al*., 2015; *Trevisan et al*., 2014; *Werner et al*., 2014]. In this context, physical models prove to be very useful, because they enable a systematic evaluation of flow regimes and heterogeneity contrasts in terms of, e.g., strength and correlation length of a permeability field. However, while studies so far have integrated heterogeneity in a simplified fashion, it has been long recognized that the complex geometrical arrangement of typical sedimentary facies plays a major role in capillary trapping [*Mikes and Bruining*, 2006; *Pickup et al*., 2000; *Ringrose et al*., 1993; *van Lingen et al*., 1996].

To address the lack of geological realism of prior experimental studies, as well as the limited dimensional size available for long-term observation of migration and trapping phenomena, a set of sandbox experiments is performed in this study on a larger (2.44 m $\times$ 0.5 m) system. The setup is unique as it enables introducing realistic subsurface conditions, thus including the presence of (a) a background hydraulic gradient, (b) significant buoyant forces, and (c) a wider continuum of heterogeneity scale. Results from two experiments are presented that have performed with surrogate fluids at ambient pressure-temperature (P-T) conditions. The first experiment is conducted in a homogeneous configuration, while the second represents a more realistic heterogeneous scenario. The scope of this experimental analysis is twofold. On the one hand, we present a bench-scale demonstration of injection schemes controlling the migration and immobilization of a surrogate CO_2 plume with and without the influence of heterogeneity. On the other hand, we provide an explicit characterization of the permeability field and boundary conditions, as well as quantification of fluid saturation distribution, for future comparison with numerical simulations. The uniqueness of these experiments lies in the ability to reproduce and observe those large-scale phenomena that control plume migration while hinting at the time scale for immobilization involved with geological heterogeneity.

2. Experimental Approach and Methods

Two experiments are presented in this study: a homogeneous setup using #50 Granusil sand and a spatially correlated, facies-based heterogeneous scenario with a log-normal distribution of permeability having

Table 1. Summary of Density (ρ), Viscosity (μ), and Interfacial Tension (γ) of Surrogate Fluids at Experimental *P-T* Conditions and Actual Fluids of $scCO_2$ and Brine at Reservoir Conditions

pPhase	ρ (kg/m^3)	μ (mPa s)	μ_{nw}/μ_w	ρ_{nw}/ρ_w	γ (mN/m)
Soltrol 220	860	4.9	0.072	0.71	15
Glycerol-water	1210	61			
$scCO_2$	266–733[a] (760[c])	0.023–0.0611[a] (0.06[c])	0.026–0.20[a] (0.075[c])	0.22–0.75[a] (0.745[c])	19.8[b]
Brine	945–1230[a] (1020[c])	0.195–1.58[a] (0.8[c])			

[a]Estimates from *Nordbotten et al.* [2005], $T = 35–155°C$, $P = 10.5–31.5$ MPa.
[b]Measurement from *Bennion and Bachu* [2006], $T = 43°C$, $P = 20$ MPa, brine salinity = 2.7 wt %.
[c]Estimates from *Singh et al.* [2010] for Sleipner field.

equivalent geometric mean $\mu_{\ln k}$ of 3.86×10^{-11} m^2 and a variance $\sigma^2_{\ln k}$ of 1.69. The two experiments presented in this study are carried out in a larger tank setup with respect to the studies by *Trevisan et al.* [2014] and *Trevisan et al.* [2015], offering the ability to recreate realistic plume spreading behavior through longer periods.

2.1. Experimental Fluids

The experiments were conducted at ambient conditions with a pair of surrogate fluids that mimic the density and viscosity contrasts of $scCO_2$ and brine at reservoir *P-T* conditions, as reported in Table 1. However, these fluids are insoluble and do not allow for study of mixing and dissolution processes. Specifically, an isoparaffinic oil (Soltrol 220) and a glycerol-water mixture (80:20 w/w) were chosen to represent the injected NWP and resident wetting-phase fluid (WP), respectively. Soltrol 220 was dyed red with Sudan IV (Fisher Scientific) and doped with 10% w/w Iodoheptane (Alfa Aesar) to allow for direct visualization of the fluid flow and to increase X-ray attenuation contrast between the two phases. Beside their immiscibility, these fluids do not undergo any long-term chemical reactions, as confirmed by negligible NWP saturation measured through X-rays attenuation before and after extended redistribution periods (1–2 months).

2.2. Experimental Aquifer Tank

Both homogeneous and heterogeneous scenarios are performed in a sand pack enclosed by a Plexiglas and aluminum tank with internal dimensions of $(244 \times 5 \times 80.8)$ cm^3. Each experiment consists of four stages: two NWP injection events separated by as many fluid redistribution (gravity relaxation) stages, during which the plume is allowed to reach hydrostatic equilibrium. Figure 1 illustrates the geometry of the tank setup and the sand arrangement for the homogeneous configuration (#50 sand for the aquifer, #8 sand for injection well and boundary layers, a fine sand mixture for the bottom and top aquitards, and a clay layer as caprock). The aquifer has a 5% slope (3° dip angle) achieved by tilting the setup during packing and a constant background WP flow is maintained in the updip direction by two constant head reservoirs connected to the coarse sand boundaries. The injection well consists of a 10 cm high acrylic pipe (internal diameter,

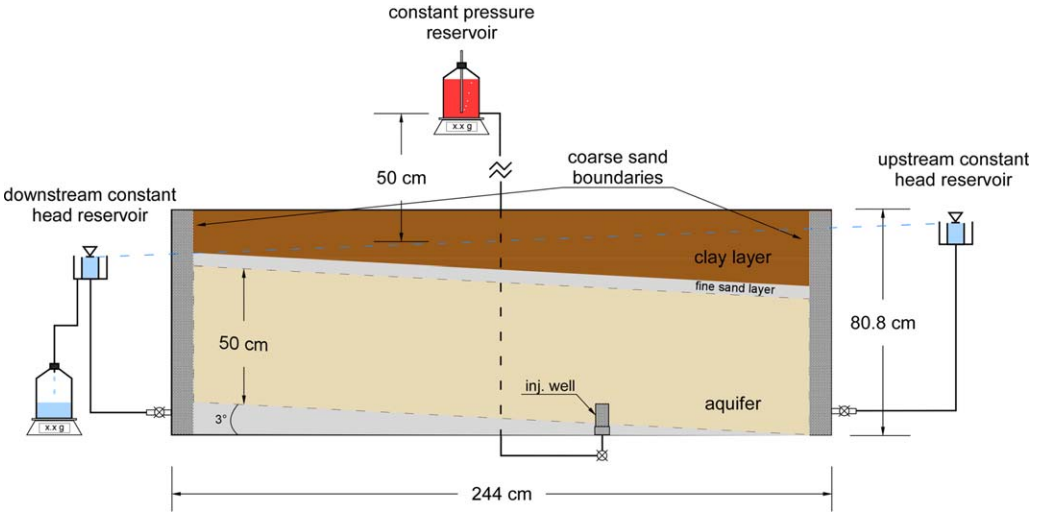

Figure 1. Schematic of the flow cell. Injection of NWP takes place from a well placed at the bottom of the aquifer. The aquifer has a gentle slope (3°) in the direction of the ambient flow (right to left). Coarse #8 sand is packed along upstream and downstream boundaries to equally constrain constant head conditions. Electronic scales continuously track NWP inflow and WP outflow masses.

I.D. = 4.5 cm) filled with #8 sand. The well is open at the top and supplied with NWP through the bottom from a constant pressure reservoir (a Mariotte's bottle) sitting on an electronic scale at $H = 50$ cm above the potentiometric surface. Since this is an inclined surface, the height difference is calculated with respect to the center of the tank. This pressure-controlled injection method was adopted for its easy implementation. However, as it will be shown in section 4, the injection flow rate resulting from this constant pressure potential condition shows fluctuations due to the influence of (1) the relative permeability of the NWP and (2) the intrinsic permeability of the sands intersected by the plume.

2.3. Design of the Heterogeneous Setup

To explicitly represent a sedimentary structure with a correlated permeability field in a synthetic aquifer, we follow the experimental approaches of *Barth et al.* [2001] and *Fernandez-Garcia et al.* [2004]. Six different sieve sizes are used to approximate a target log-normal distribution of the facies-based permeability field and populate a two-dimensional rectangular array of 122 by 25 cells with dimensions (2×2) cm^2. The six categories (or facies) correspond to Granusil silica sands #16, #20, #30, #50, #70, and #110, from coarsest to finest, spatially arranged as shown in Figure 2a (see Table 2 for physical properties of the sands). Figure 2b shows the target histogram of ln$k$ values for the six facies populating the permeability field (except for #8 sand used for boundaries and wells). Their volumetric fractions are: 3%, 11.4%, 19.5%, 30.8%, 24.6%, and 10.7%, respectively, following the log-normal distribution of permeability. The moderate permeability contrast of the experimental setup is used to shorten the experimental time by facilitating faster plume migration compared to actual reservoirs.

In order to compare the degree of heterogeneity of the synthetic reservoir with cases of practical interest, we estimate the permeability variation using the Dykstra-Parson coefficient V_{DP} [*Craig*, 1993]:

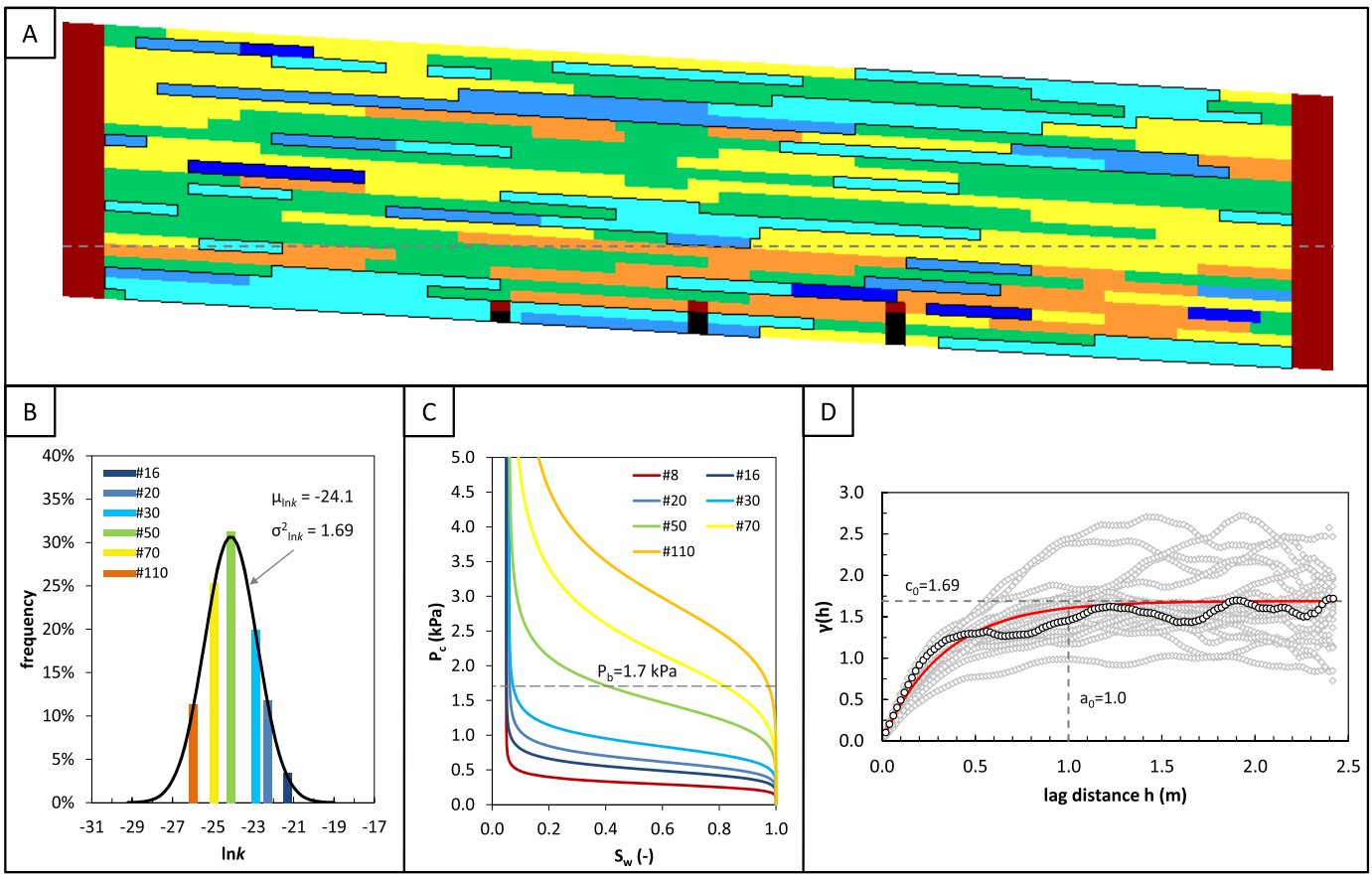

Figure 2. (a) Spatial arrangement of the six sand categories in SIS realization #18, with highlighted high-k clusters (dashed line represents X-ray detection edge); (b) target histograms for the six sands representing a ln$k$ distribution (k in m^2); (c) characteristic $P_c(S)$ drainage curve for each sand, including #8 sand used for lateral boundaries and wells; (d) theoretical (red line) and experimental (symbols) variograms for 20 realizations of the permeability field; the black variogram represents the realization selected for the packing setup (#18).

Table 2. Physical Properties of the Silica Sand Grades Used in the Experiments From *Sakaki and Illangasekare* [2007]

Material ID	Sieve Size	k (m^2)	ln$k$	φ_{avg} (–)	d_{50} (mm)	d_{60}/d_{10} (–)
1	#16	5.62×10^{-10}	−21.3	0.397	0.88	1.72
2	#20	2.14×10^{-10}	−22.3	0.41	0.7	
3	#30	1.23×10^{-10}	−22.8	0.433	0.5	1.50
4	#50	3.37×10^{-11}	−24.1	0.4	0.3	1.94
5	#70	1.43×10^{-11}	−25.0	0.44	0.2	1.86
6	#110	5.21×10^{-12}	−26.0	0.38	0.12	∼2.0

$$V_{DP} = \frac{k_{50} - k_{84.1}}{k_{50}} = 1 - e^{-\sigma} \quad (1)$$

where k_{50} is the mean permeability and $k_{84.1}$ is the mean permeability plus one standard deviation; for a homogeneous reservoir V_{DP} approaches zero, while for an extremely heterogeneous reservoir V_{DP} would approach one. For this study, V_{DP} is 0.73, which is representative of most reservoirs [*Behzadi and Alvarado*, 2012; *Farajzadeh et al*., 2011; *Kumar et al*., 2005; *Saadatpoor et al*., 2010; *Tchelepi and Orr*, 1994; *Tian et al*., 2016]. Another metric often considered is the variance of ln$k$ ($\sigma^2_{\ln k}$). In this study, a variance of 1.69 is selected, falling in the range of values (0.2–5) reported by a number of modeling studies relevant to GCS [*Cameron and Durlofsky*, 2012; *Deng et al*., 2012; *Flett et al*., 2004; *Han et al*., 2010; *Lengler et al*., 2010].

Capillary pressure $P_c(S)$ drainage curves of the sands cover a range of capillary entry pressures between 0.28 and 2.04 kPa (Figure 2c). These values define the ability of NWP to invade a given sand, while the final saturation in each sand is controlled by the so-called buoyancy pressure, P_b, exerted by the height difference H between the injected NWP and the resident WP during the injection (50 cm):

$$P_b = (\rho_w - \rho_{nw})gH \quad (2)$$

where ρ_w and ρ_{nw} are the densities of WP and NWP, respectively, and g is the gravitational constant. For simplicity, equation (2) defines P_b at the injection point, where it takes a value of 1.7 kPa, which is estimated using $H = 50$ cm. Since this in an open system, as the plume moves upward, this initial buoyancy pressure will dissipate proportionally to its vertical location.

The spatial sand distribution is designed to mimic a layered structure that recreates a permeability field in agreement with most reservoir simulations [e.g., *Deng et al*., 2012; *Flett et al*., 2007; *Han et al*., 2010; *Saadatpoor et al*., 2010; *Tian et al*., 2016]. The Sequential Indicator Simulation (SIS) algorithm [*Journel and Alabert*, 1990] combined with the open source program SGeMS [*Remy et al*., 2009] is used to generate 20 equiprobable realizations based on an exponential variogram (equation (3)):

$$\gamma(h_i) = c_0\left[1 - \exp\left(-\frac{3h_i}{a_{0,i}}\right)\right] \quad (3)$$

where c_0 is the sill, h_i is the lag distance in the i direction (x, z), and $a_{0,i}$ is the range. The correlation length is defined as $\lambda_i = a_{0,i}/3$. The layered structure is built by assigning long horizontal (100/3 cm) and shorter vertical (4/3 cm) correlation lengths as input parameters for SIS simulations. Figure 2d shows the experimental variograms along the flow direction for 20 SIS realizations (gray symbols), highlighting the theoretical variogram (red line) and realization 18 (black symbols).

Prior to injection, the porosity variation of the sand pack was determined for both homogeneous and heterogeneous packing configurations by measuring X-ray attenuation across the flow domain (supporting information Figure S.I. 1). Since the sands have all similar porosity (∼0.4), their spatial distribution is not distinguishable from this contour plot; however, the evidence of an inclined stratification, as well as of the clay layer confining the aquifer (porosity > 0.5) is clear. The higher average porosity observed in the heterogeneous case is due to the looser packing carried out to minimize the mixing of finer and coarser sands.

2.4. Boundary Conditions

A constant pressure ($P_b = 1.7$ kPa) boundary condition is applied at the injection well (see Figure 1). The target volume for each injection is 1 L, corresponding to approximately 0.044 pore volumes (estimated using extents of the aquifer multiplied by average porosity; 229 cm × 5 cm × 50 cm × 0.4). Interestingly, even though both experiments share the same injected volume, the injections exhibit variable flow rate and therefore different duration. This behavior is further discussed in section 4.3.

Prior to NWP injection, different background hydraulic gradients were tested to mimic the effect of regional groundwater flow through deep saline aquifers [*Larkin*, 2010], as shown in Figure 3. For the heterogeneous

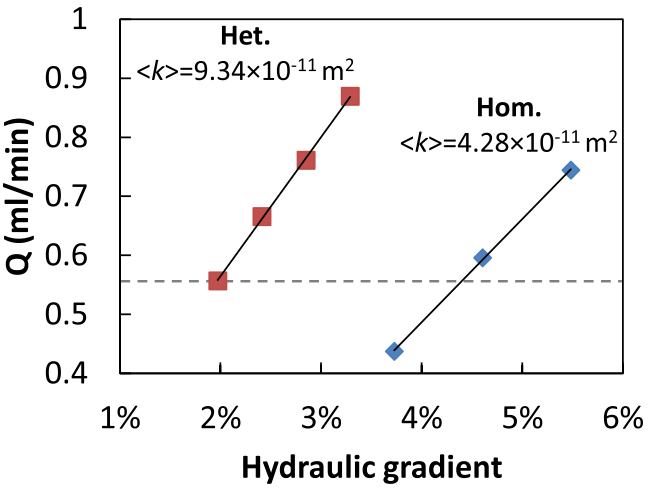

Figure 3. Correlation between background hydraulic gradient and outflow rate Q (dashed line represents the 0.56 mL/min wetting phase flow discharge applied to both experiments).

scenario, a 4.5 cm head difference across the domain was selected, resulting in a WP flow discharge of 0.56 mL/min at the left boundary and corresponding to a 2% hydraulic gradient. The latter was increased to 4.5% in the homogeneous scenario to maintain a similar WP flow discharge. This comparison shows the direct manifestation of the presence of high-permeability layers channeling the flow in the heterogeneous setting, as the estimated effective permeability for the heterogeneous case is 9.34×10^{-11} m^2 and twice of the permeability for the homogeneous case (4.28×10^{-11} m^2).

2.5. Successive Drainage and Imbibition Experiments

For each sand-packed large tank (homogeneous or heterogeneous), the experiment includes the first injection event with a target NWP volume of 1 L, the first redistribution (or imbibition) event with no injection, the second injection event with the same volume, and the second redistribution event. Each of the redistribution events stops when no further movement of the plume is observed along horizontal and vertical directions. The design of these experiments aims to assess long-term migration and trapping of NWP in the meter-scale system, providing a necessary dataset for understanding field-scale processes of $scCO_2$ migration and trapping. The reservoir thickness used in this study is only one order of magnitude smaller than that for some pilot and demonstration GCS projects. For example, the Frio C sand used for CO_2 injection in the Frio pilot test is ~5 m thick.

Central to the experimental approach is the use of X-ray attenuation to measure the spatial and temporal distribution of the phase saturations in the sand pack noninvasively and with high spatial resolution (one measure every 15 mm in x and z directions). The saturation measurements represent a depth-average along the second horizontal axis (y) and an areal average over a sampling volume determined by the radius of the collimated X-ray beam (1 mm). These measurements have an average detection error of $\pm$1.5%. Further details about the X-ray attenuation device, both hardware-wise and software-wise, as well as the procedure for X-ray data conversion into actual phase path-lengths can be found in *Trevisan et al*. [2014] and *Trevisan* [2015]. In conjunction with X-ray attenuation measurements, photographic images of the transparent walls of the flow cell are continuously gathered in order to discard any preferential flow of NWP along the vertical walls.

3. Experimental Results

To show the effect of known heterogeneity structures on migration and trapping of NWP fluid, we present experimental observations for both homogeneous and heterogeneous setups in a similar fashion. Figures 4 and 5 illustrate the development of NWP plumes qualitatively, with photography, and quantitatively, with saturation contours gathered via X-ray attenuation, for these experiments. For the sake of conciseness, only plume snapshots acquired at the end of the injection and redistribution stages are presented, while a more complete set of results at additional times is available as supplemental material (supporting information Figures S.I. 1 and Figure S.I. 2). The tables embedded in Figures 4 and 5 summarize the NWP mass balance corresponding to each snapshot. The NWP volumes are broken down into inflow, outflow, detected plume (above $z = 0$), and undetected plume (below $z = 0$) volumes within the sandbox. As a comparative measure between the two scenarios, we introduce a trapping efficiency factor, $\varepsilon = V_{plume}/V_{inflow}$, to represent the fraction of NWP (detected and undetected) that remains in the domain with respect to the total amount injected. Additionally, we introduce the perimeter-to-area ratio (P/A) as an indicator of plume surface available for dissolution and chemical reactions.

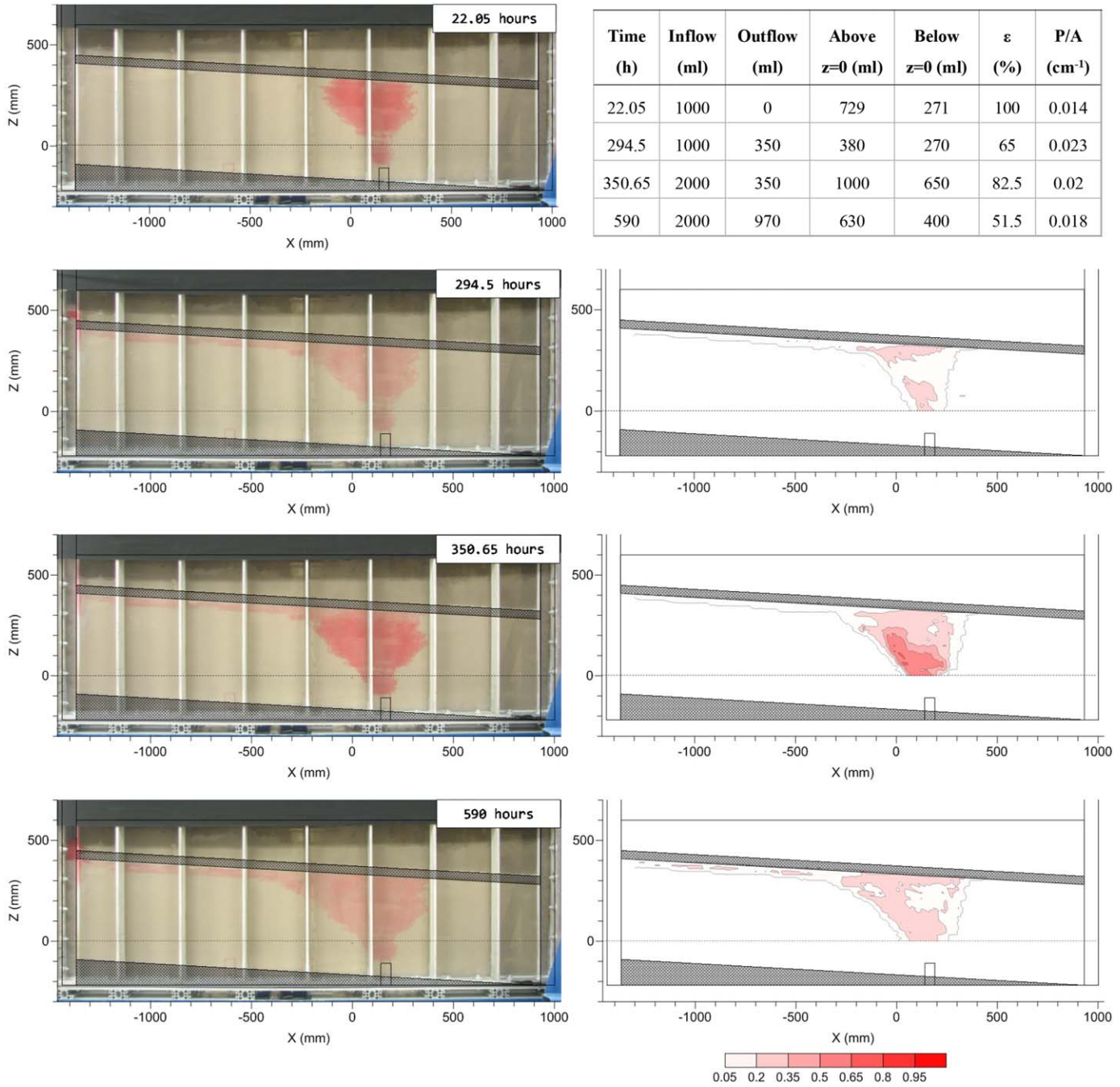

Time (h)	Inflow (ml)	Outflow (ml)	Above z=0 (ml)	Below z=0 (ml)	ε (%)	P/A (cm^{-1})
22.05	1000	0	729	271	100	0.014
294.5	1000	350	380	270	65	0.023
350.65	2000	350	1000	650	82.5	0.02
590	2000	970	630	400	51.5	0.018

Figure 4. (left) Homogeneous base case experiment: plume snapshots taken via photography and (right) X-ray attenuation at the end of each stage: first injection (first row), first redistribution (second row), second injection (third row), and second redistribution (fourth row). Total NWP volumes corresponding to each snapshot are listed in the table. Temporal evolution of NWP saturation at five observation points is provided in the supporting information.

3.1. Homogeneous Scenario

The homogeneous experiment is designed to represent the simplest setting for a buoyant plume to migrate through a porous domain. The purpose of this fairly simplistic setup is twofold: (1) to observe plume behavior during successive drainage and imbibition events, which could be used in the future for testing two-phase flow models considering the effect of hysteresis, and (2) to provide a control experiment to compare with a more complex permeability field. To facilitate the comparison between both scenarios, we analyze each of the four stages separately.

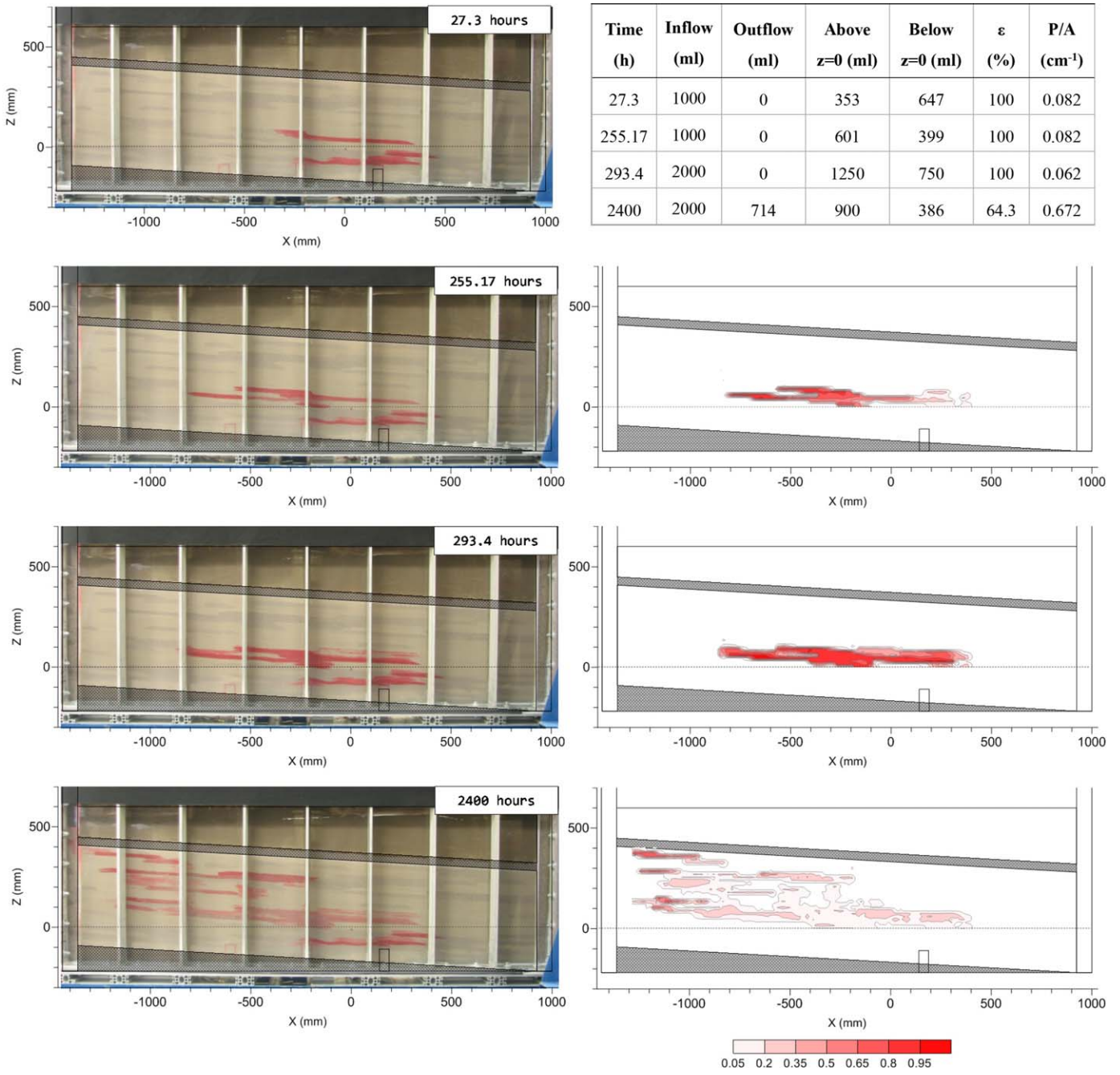

Time (h)	Inflow (ml)	Outflow (ml)	Above z=0 (ml)	Below z=0 (ml)	ε (%)	P/A (cm^{-1})
27.3	1000	0	353	647	100	0.082
255.17	1000	0	601	399	100	0.082
293.4	2000	0	1250	750	100	0.062
2400	2000	714	900	386	64.3	0.672

Figure 5. (left) Heterogeneous experiment: plume snapshots taken via photography and (right) X-ray attenuation at the end of each stage: first injection (first row), first redistribution (second row), second injection (third row), and second redistribution (fourth row). Total NWP volumes corresponding to each snapshot are listed in the table. Temporal evolution of NWP saturation at five observation points is provided in the supporting information.

First Injection Stage (0–22.05 h, Figure 4, top row): early evolution of the plume appears to be controlled by buoyancy force, showing a chimney-like structure, which gradually develops into an asymmetrical shape, driven by the background WP flow from right to left. Since the plume reaches the caprock at the same time the injection is halted, the influence of aquifer dip on plume geometry is minimal during this stage. Also, toward the completion of this stage, the displacement front shows some unstable behavior characterized by several short-range fingers, possibly due to the buildup of the injection flow rate, causing viscous forces to dominate over capillary forces. The plume at the end of this stage is referred to "early plume," and the saturation (i.e., maximum initial saturation for later imbibition) in this plume under drainage is relatively high.

First Fluid Redistribution Stage (22.05–327.27 h, Figure 4, second row): once the first injection is complete, the plume is allowed to redistribute until it approaches equilibrium, which is considered when no further movement of the plume is observed along horizontal and vertical directions (as shown in section 4). During this buoyancy-dominated relaxation process, the plume (i.e., the postinjection plume) develops predominantly along a thin layer underneath the caprock and leaves behind a trail of residual saturation. Approximately 11 days after the injection ends, 35% of the injected mass has escaped out of the aquifer and the postinjection plume takes an average NWP saturation of 17%. Interestingly, this residually trapped saturation is not homogeneously distributed within the plume, as shown by the X-ray contour maps, where values range between 5% and 20%. The highest saturation of trapped NWP occurs in the footprint of the early plume event and can be attributed to the high initial saturation within this footprint. Out of this footprint, the postinjection plume experiences drainage and imbibition during the redistribution period, and has much smaller initial maximum saturation (than that in the early plume at the end of the first injection event) that results in even smaller saturation of trapped NWP. These results indicate that the observed behavior of trapped NWP may be represented by existing empirical [e.g., *Land*, 1968] or nonempirical trapping models [e.g., *Cihan et al*., 2014, 2016]. The irregular saturation distribution within the footprint of the early plume probably results from the imperfect nature of the sand packing causing water encroachment to occur by nonuniform displacement/imbibition. Although the behavior observed here has been predicted at the reservoir scale by several continuum-based multiphase flow models [*Flett et al*., 2007; *Kumar et al*., 2005; *Lengler et al*., 2010], no experimental evidence has been yet reported with such detailed characterization of the saturation distribution.

Second Injection Stage (327.27–350.65 h, Figure 4, third row): during early times of the second injection event, the plume follows the path established by the previous injection event. However, before the target injection volume is reached, the lateral spreading of the plume increases resulting in a wider footprint than the early plume, as well as larger median plume saturation (0.46 versus 0.38), as shown in Figure 7. The larger spreading and higher saturation are most likely due to (1) the presence of trapped NWP in the early plume that has a detrimental effect on relative WP permeability as compared to the nearby NWP-free regions, (2) right-to-left background WP flow that results in the skewness of the plume, and (3) the dynamic evolution with additional injection that would occur for the same continuously injected volume of 2 L. All these effects cannot be distinguished by the only one data set without comparison.

Second Fluid Redistribution Stage (350.65–590 h, Figure 4, bottom row): the positive impact of a second injection event is revealed by the area occupied by the plume after the second redistribution, which is 23% larger than the area occupied after the first injection and redistribution. Consequently, a larger footprint enables a 58% increase in residually stored mass. On the other hand, this experiment shows the principal disadvantage of homogeneous and isotropic reservoirs, where gravity segregation causes the plume to bypass a large fraction of the reservoir. From the NWP saturation contour maps obtained with X-ray attenuation, a concave region of lower saturation surrounded by relatively higher saturation can be observed, as a possible effect of the background WP flow on plume trapping. Similar effects on the inhomogeneity of the trapped saturation distribution as for the first redistribution, but the region with higher residual saturations seems to be larger.

Note that the plume is always continuous in its footprint at the different stages of the experiment. The trapping efficiency factor after the second redistribution stage is 51.5%, smaller than 65% after the end of the first redistribution stage. However, a NWP volume of 1030 mL is trapped within a wider plume, larger than the total trapped volume of 650 mL after the first redistribution stage.

3.2. Heterogeneous Scenario

First Injection Stage (0–27.3 h, Figure 5, top row): as opposed to the homogenous scenario, where the plume freely migrates upward and reaches the caprock by the end of the first injection event, the presence of capillary and permeability barriers of finer sands in the heterogeneous scenario leads to a 44% reduction in vertical migration distance and a 66% increase in horizontal migration distance. The injected NWP fluid migrates into a cluster of connected coarse sands (#16, #20, #30) that is immediately above the injection well and bounded by fine #110 sand from the left and right sides and by #70 sand from the top of the cluster (see Figure 2a). With time, the injected NWP fluid accumulates in this high-permeability cluster, pools under the overlying less permeable #70 sand, and migrates downward to the left side following the

structure of the coarse sands. This results in an increase in plume thickness and thus NWP pressure at the top of this NWP pool. When the NWP pressure at the bottom of #70 sand is higher than its entry capillary pressure (∼1.2 kPa), the capillary barrier is broken and NWP starts to migrate upward through the #70 sand into the second cluster of coarse sands to form the second pool of NWP. Clearly, the plume includes two separate pools connected by a flow path through #70 sand where NWP saturation is small. However, it is this low-saturation flow path that supplies all NWP mass in the second, upper pool. The second cluster consists of #30 sand and #16 sand to the left and is bounded from the top by a continuous layer of #70 sand crossing over the entire sandbox length. At the end of this stage, the second pool is filled by NWP only in the #30 sand portion of this cluster. This accumulation-penetration-breakthrough phenomenon was simulated for stratified intraformation layers for the Illinois Basin [*Birkholzer and Zhou*, 2009; *Zhou et al*., 2010], but this phenomenon is shown for the first time in a laboratory experiment with sufficient aquifer thickness.

First Fluid Redistribution Stage (27.3–262.42 h, Figure 5, second row): at the end of this stage, all injected NWP mass is trapped within the two pools by capillary barriers of the surrounding finer sands and local residual saturation in the two clusters of coarse sands. With time, the first, lower pool shrinks a little bit and its saturation decreases, leading to the reduction in NWP pressure at the top of the pool. The reduced NWP mass from the lower pool migrates through the #70 sand flow path into the second, upper pool. At the end of this stage, the flow through this path ceases because at the bottom of this path, the continuous reduction in the NWP pressure and saturation leads to the balance between capillary force of the finer sand and buoyancy force from the lower pool. The capillary barrier of the fine #70 sand is recovered from its broken condition, trapping large amount of NWP mass in the lower pool with higher saturation than local residual saturation (∼20%). With continuous inflow from the lower pool and redistribution in the upper pool, NWP fluid migrates updip to the left side and fills in a new branch of #16 sand facies. At the end of this stage, the saturation distribution in the upper pool follows the balance between capillary and buoyancy forces at any location of the pool. Due to the updip feature of the cluster and the pool, buoyancy-induced NWP pressure is the highest at the upper end of the pool on the left and lowest on the lower end of the pool on the right, resulting in the saturation variability in the pool.

The entire upper pool is trapped by the capillary barrier of the overlying continuous #70 sand layer, as the highest NWP pressure at the upper-left end of the pool is still lower than the entry capillary pressure of #70 sand. The upper pool is also surrounded by finer #50 sand on its left side and #50 and #70 sands on the right side of the pool. This phenomenon of a NWP pool of high saturation trapped in a "pocket-shaped" cluster of high-permeability sands by surrounding lower-permeability sands or shales on all sides (at least top and updip) except one in-flow side is referred to as "pocket" trapping. The in-flow side can be the downdip or bottom side through which NWP fluid or $scCO_2$ is supplied. The pocket trapping is caused by capillary and permeability barrier effects along the semi-closed boundary of the trapped NWP pool. This trapping is similar to the dead-end effect in contaminant transport [*Coats and Smith*, 1964] and hydrocarbon trapping in anticlines.

Second Injection Stage (262.42–293.42 h, Figure 5, third row): the lower cluster of coarse sands and the lower NWP pool is additionally charged by injected NWP fluid, leading to an increase in NWP saturation in this pool. The increased saturation leads to higher capillary pressure at the top of the pool and the bottom of interpool #70 sand, breaking the capillary barrier again. Once the interpool flow path is reactivated for flow, the NWP pressure at the top of the upper pool increases sharply because the entire plume (i.e., the two pools and the interpool flow path) is connected, leading to much higher NWP columns. This higher NWP pressure drives NWP upward migration into the #50 sand facies overlying the #30 sand in the downdip portion and overlying the #16 sand in the updip portion of the upper pool.

Second Fluid Redistribution Stage (293.42–2400 h, Figure 5, bottom row): with time of redistribution, NWP migrates updip further in the #50 sand from the #16 branch to expand the second pool. Meanwhile, the NWP pressure is sufficiently high at the updip ends of the pool, and thus breaks the capillary barrier of the continuous #70 sand layer at two locations. The newly created two flow paths through #70 sand facilitate upward migration of NWP to form the third pool in the third cluster of #20, 30, and #50 sand. The same accumulation-penetration-breakthrough process continues to create the fourth and the fifth NWP pool. The fifth pool is connected to the left-side boundary, resulting in outflow of 35.7% of the injected mass from the sandbox.

This last stage takes 2.9 months to reach quasi-hydrostatic equilibrium. 64.3% of the injected NWP is immobilized within the aquifer, a 12.8% increase with respect to the homogeneous scenario. Another significant feature of the plume is its specific surface area, represented by the P/A ratio, showing a 10-fold increase with respect to the end of the first redistribution stage, and a 37-fold increase with respect to the end of the second redistribution stage for the homogeneous scenario.

Note that the contrasts of permeability and entry capillary pressure among the six sand facies are chosen to show all the physical processes and phenomena, including pooling under finer facies and capillary barrier effect, breakthrough of capillary barriers caused by buoyancy-enhanced NWP pressure, start and cessation of interpool NWP flow, and cyclic drainage and imbibition. These contrasts are also chosen to show residual trapping, hysteresis caused by cyclic drainage and imbibition, and pocket trapping that mainly depends on the heterogeneity structures. These chosen contrasts make this unique experiment feasible at the time scale of 100 days and the spatial scale of 244 cm $\times$ 80.8 cm $\times$ 5 cm. The physical processes and phenomena and the trapping mechanisms demonstrated in the experiment are relevant to the field-scale GCS reservoirs that have much higher contrasts of permeability and entry capillary pressure. The higher contrasts will facilitate some phenomena, such as pocket trapping.

4. Discussion

Some important observations made in the homogeneous experiment include: (1) the linear increase in injection flow rate with time under the constant injection pressure condition, and the subsequent development of displacement front instabilities, (2) the absence of remobilized NWP during the second injection and the larger footprint achieved afterward, and (3) the nonuniform NWP saturation distribution within the early plume footprint. The heterogeneous experiment provides the following observations: (1) the absence of CO_2 outflow after the first fluid redistribution, and (2) the longer time of plume redistribution (2.8 months). Some of these observations in the two experiments cannot be predicted by the state-of-the-art mathematical models, thus offering an opportunity to improve these models.

4.1. Spatial Moment Analysis

Besides visual observations and quantitative measurement of plume saturation via X-ray attenuation, we assess the spreading of the plume throughout the various stages of the experiments via analysis of spatial moments [*Eichel et al.*, 2005; *Fagerlund et al.*, 2007; *Han et al.*, 2010; *Kueper and Frind*, 1991]. For an immiscible plume, the zeroth moment, M_{000}, is defined in a similar manner as for a solute concentration [*Freyberg*, 1986]:

$$M_{000}(t) = \sum_i \varphi^i(x,y,z) S^i_{NW}(x,y,z,t) V^i \tag{4}$$

where φ^i is the porosity (space-dependent) and S^i_{NW} is the space-dependent and time-dependent NWP saturation for the ith gridblock with volume V^i. The first moments in the x direction and z direction normalized by the total NWP volume present in the domain (M_{000}) define the coordinates of the plume centroid:

$$x_c(t) = \frac{M_{100}}{M_{000}} = \frac{\sum_i x^i \varphi^i(x,y,z) S^i_{NW}(x,y,z,t) V^i}{\sum_i \varphi^i(x,y,z) S^i_{NW}(x,y,z,t) V^i} \tag{5}$$

$$z_c(t) = \frac{M_{001}}{M_{000}} = \frac{\sum_i z^i \varphi^i(x,y,z) S^i_{NW}(x,y,z,t) V^i}{\sum_i \varphi^i(x,y,z) S^i_{NW}(x,y,z,t) V^i} \tag{6}$$

4.1.1. Zeroth Moment

A critical problem related to the long-term containment of CO_2 in deep reservoirs and recently tackled by tracer tests is the assessment of the amount that is being retained under residual saturation conditions [*LaForce et al.*, 2014; *Myers et al.*, 2015; *Rasmusson et al.*, 2014]. In fact, any part of the plume occurring at saturations higher than residual is considered mobile and susceptible to further displacement, unless additional trapping mechanisms, such as dissolution trapping and pocket trapping, get underway. The controlled laboratory experiments in conjunction with a refined X-ray scanning grid allow for accurate quantification of the total NWP volume present in the tank using zeroth moment calculations. To evaluate the effects of capillary barriers and sequential injections on the retention of NWP we selected a cutoff value of 0.22 to differentiate mobile and residual fractions of a saturation at local scale. This cutoff value represents the maximum residual NWP saturation of the homogeneous experiment; however, this cutoff value is higher than

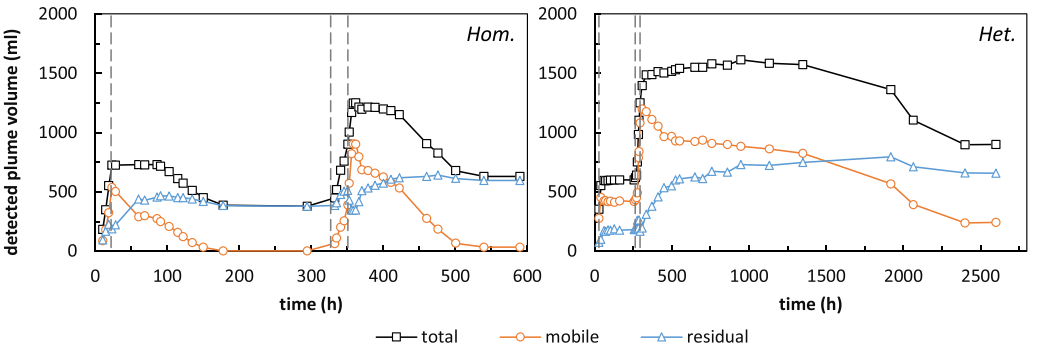

Figure 6. Zeroth moment evolution representing total plume volume (detected by X-ray scanning) during both experiments (black squares). Orange circles and blue triangles differentiate mobile and residual portions of the plume, respectively. Dashed lines delineate the two injection events.

actual residual saturation values owing to the hysteretic behavior of the $P_c(S)$ relationship [*Cihan et al.*, under review], and may result in slight over-prediction of the immobile volume and under-prediction of the mobile volume.

As shown in Figure 6, both experiments reach an apparent hydrostatic equilibrium at the end of the experiments as no further changes in the trapped NWP mass (mobile and immobile) are observed. The final residually trapped volumes are similar for the homogeneous and heterogeneous cases, 595 mL and 657 mL, respectively. However, the final mobile volume (243 mL) in the heterogeneous case is significantly larger than that (34 mL) in the homogeneous case, because of local structural "pocket" trapping caused by heterogeneity structures and capillary barrier effects. In addition, the heterogeneity elongates the time (3.6 months) needed for plume stabilization after two injection events, much longer than that (24 days) for the homogeneous cases.

In addition to the analysis of total plume volume, assessing the range of NWP saturations measured at the end of each stage provides information about the trapping capacity of each scenario (Figure 7). At the end of both injection stages (stages A and C), capillary barriers have a dominant effect on plume migration in the heterogeneous scenario, leading to the highest saturations after the second injection. After the first fluid redistribution (stage B), the mobile NWP fluid exists over 70% of the plume footprint under pocket trapping in the heterogeneous case, while a residual (immobile) saturation state has been reached in 99% of the plume footprint in the homogeneous case. Finally, at the experiment completion (stage D), the main difference in terms of saturation distribution between both scenarios is the presence, although scattered, of high saturation areas in the heterogeneous case.

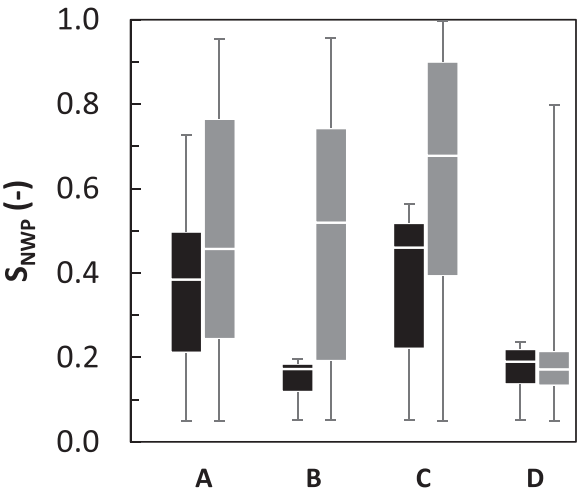

Figure 7. NWP saturation distributions measured at the end of each stage for both experiments (black for homogeneous, gray for heterogeneous). (a) end of first injection; (b) end of first redistribution; (c) end of second injection; (d) end of second redistribution.

4.1.2. First Moment

The analysis of first spatial moments allows tracking the position of plume's centroid in the *x-z* plane during the temporal evolution of the NWP plume. As shown in Figure 8, whenever the plume breaks through at the outflow boundary, the center of mass reverses its original migration direction (both horizontally and vertically) and starts moving countercurrent with respect to the dipping angle of the aquifer and the background flow. This characteristic behavior is observed in both scenarios and during both injection events. In the homogeneous scenario, the observed behavior is essentially identical during the two injection events. In the

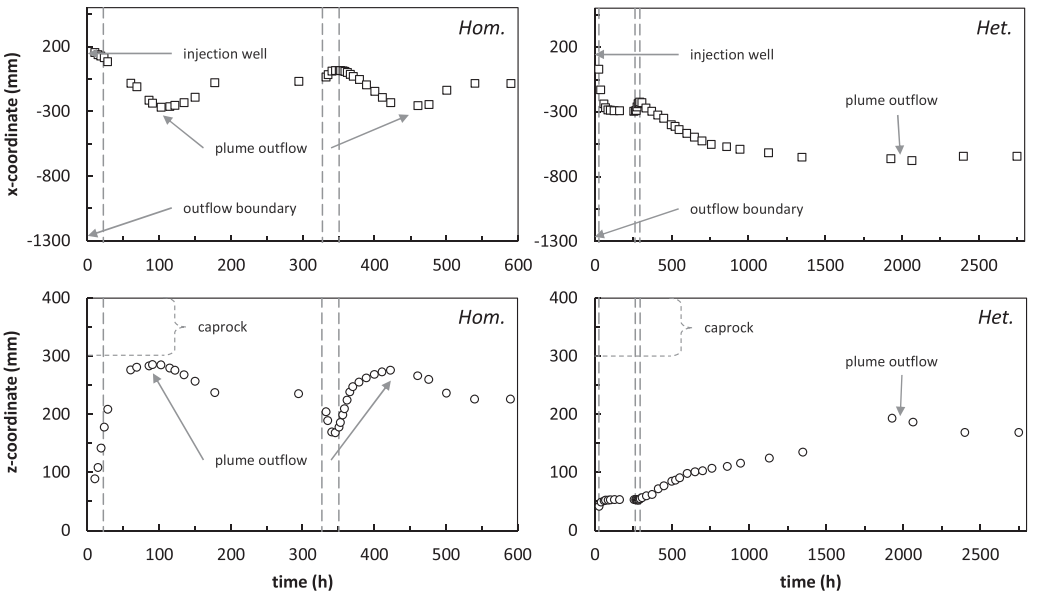

Figure 8. Temporal evolution of the horizontal (squares, top row) and vertical (circles, bottom row) coordinates of the plume center of mass during both experiments. The intervals shown by the vertical dashed lines represent the duration of the injection events. X-coordinates decrease toward the left (outflow) boundary of the domain. Z-coordinates of caprock vary from 300 mm (right boundary) to 400 mm (left boundary).

heterogeneous scenario (right column in Figure 8), however, an overall equilibrium is quickly attained after the first injection, both horizontally and vertically, while after the second injection event, a slower upward, left-bound movement of the plume centroid takes place for approximately two months, culminating with the breakthrough into the outflow boundary.

Another interesting observation is that in the homogeneous scenario the plume remains very close to the caprock, as compared to the heterogeneous scenario. This behavior could have important implications in actual field conditions, where avoiding a prolonged seal exposure to CO_2 may prevent mineral reaction that can undermine its geological integrity.

4.2. Assessment of Flow Regimes

As the primary objective of this type of experiments is to mimic flow behavior of a $scCO_2$ plume through a brine-saturated aquifer, the injection flow rate was maintained inside the limits of capillary/buoyancy-dominated flow regime. Evidence from laboratory [*England et al.*, 1987] and field observations [*Cavanagh and Haszeldine*, 2014] suggest that for capillary number ($Ca = U_i \mu_i / \gamma$) $< 10^{-5}$, buoyant fluids such as oil or CO_2 move across the porous medium via gravity-driven ganglia and therefore can be modeled with numerical methods that neglect viscous forces, such as invasion percolation [*Frette et al.*, 1992; *Meckel et al.*, 2015]. For the experiments presented here, we estimate capillary numbers with two different methods: (1) from NWP velocity (flow rate/well area) during the injection and (2) from plume's center of mass velocity (traveled length/time) during the fluid redistribution stages. Although the second method to estimate NWP characteristic velocity may seem unconventional, the absence of a specific NWP flow rate during fluid redistribution stages required a measure of average displacement velocity of the plume centroid. The evolution of the capillary number presented in Figure 9 points toward similar injection flow regimes for both experiments and higher influence of capillary forces (smaller Ca) during gravity relaxation for the heterogeneous scenario. To compare the magnitude of buoyancy and capillary forces, we estimated the Bond number ($Bo = \Delta\rho g k / \gamma$) using #50 sand to represent the permeability of both homogeneous and heterogeneous aquifers. The resulting Bond number ($Bo = 7.71 \times 10^{-6}$) is an order of magnitude higher with respect to the Utsira formation ($Bo = 1.74 \times 10^{-7}$) [*Singh et al.*, 2010]. A further assessment between buoyancy forces and viscous forces can be realized by calculating the ratio *Bo*/*Ca*, also known as Gravity number, which trend is inversely proportional to that of *Ca*.

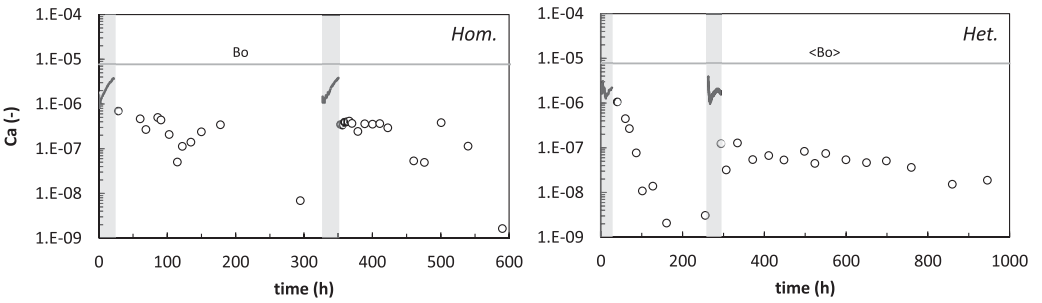

Figure 9. Evolution of the capillary number during homogeneous (left) and heterogeneous (right) experiments. Calculations of NWP velocity are based on injection flow rate (continuous lines) and average displacement velocity of plume centroid (circles). Bond number is calculated using permeability of the homogeneous aquifer (Bo) and average permeability of the heterogeneous aquifer (⟨Bo⟩). Shaded areas represent injection periods. For visualization purposes, the length of the heterogeneous plot was reduced from 2500 to 1000 hours.

4.3. Injection Flow Rate Evolution

For the homogeneous experiment (Figure 10, left column), the first and second injection events take 22 and 23 h to complete the target injection volume of 1 L. For both injection events, the flow rate rose monotonically from 0.31 to 1.16 mL/min. This behavior could be explained by near-well enhanced NWP relative permeability caused by saturation increase with time and by the growth of the plume in both length and width.

For the heterogeneous experiment (Figure 10, right column), the injection duration extends to 27 and 30 h during the first and second injection events. During the first injection, the flow rate shows several rapid changes indicating a strong influence of the permeability structure. The higher rate during the first 10 h indicates easy injection into the first cluster of high-permeability sand facies (see Figure 2a) with the lower plume pool as shown in the first row of Figure 5. The later behavior of the injection rate with a decrease and then a gradual increase indicates the impact of low-permeability sand (#70) that is broken through by NWP to form the upper plume pool. The smaller fluctuations of the injection rate show the impacts of smaller-scale structures of permeability within each cluster. For the second injection event, the injection rate decreases sharply and then increases gradually, showing a smoother evolution. This behavior of the injection rate clearly shows the control of the low-permeability sand between the two clusters of high-permeability sands. The quick reduction can be attributed to this structure because the high saturation in the lower pool remains stable during the first redistribution stage and thus does not change the relative permeability significantly. At later time of injection, the rate is similar for both injection events because the

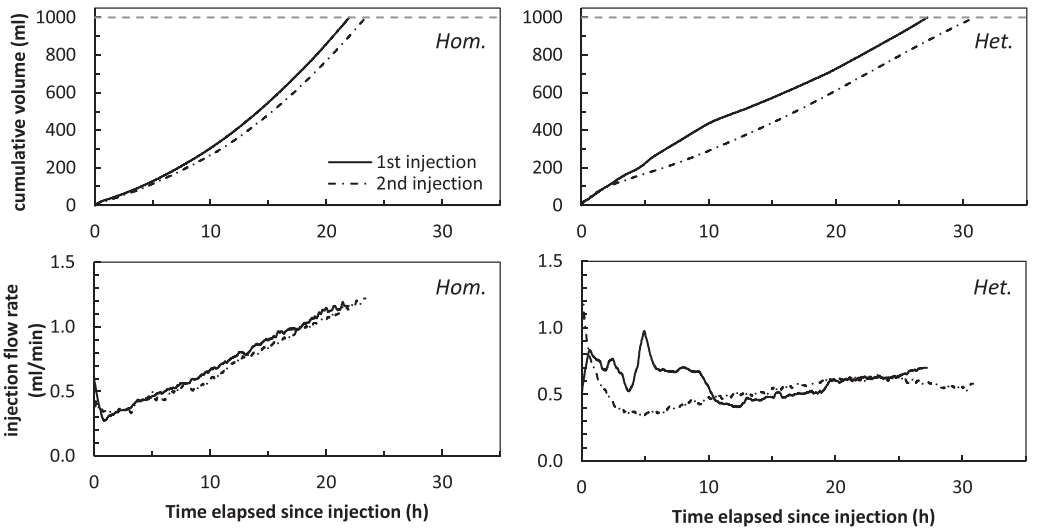

Figure 10. Evolution of cumulative inflow volume (top row) and flow rate (bottom row) of Soltrol 220 for the homogeneous (left column) and heterogeneous (right column) experiment. Target injected volume (1000 mL for each injection event) is highlighted by horizontal dashed lines for cumulative volumes.

flow paths connecting the two pools are also stable in terms of saturation and relative permeability. Overall, the evolution of the injection rate depends on the absolute permeability, saturation-dependent relative permeability and the structure of absolute permeability that controls the pools of plume. It will be very interesting to use numerical modeling to match the observed flow rates with all known heterogeneity structures and plume evolution with quantified high-resolution saturation.

4.4. Comparison With Small-Tank Experiments

The immiscible displacement experiments, referred to as large tank experiments, performed in the 2.4 m × 0.5 m sandbox represent the last iteration of the experimental analysis on capillary trapping that originated from smaller (0.7 m × 0.16 m) and less complex setups [*Trevisan et al*., 2015, 2014]. To reiterate the improved convenience of these experiments with respect to previous, smaller and simpler setups, the increased size of the synthetic reservoir allows to recreate plume geometries and injection volumes that are more realistic. Consequently, with respect to previous small tank experiments, the progression to the current large tank system involves four main additional features: (1) a larger influence of buoyancy forces, enabled by a lower aspect ratio of the aquifer; (2) the implementation of a background hydraulic gradient; (3) the sequential injection scheme and cyclic drainage and imbibition; (4) a larger variability of the permeability field. These features, in addition to the meter-scale system and long-term monitoring, make some of the observations discussed above unique and first of the kind.

5. Concluding Remarks

The large tank experiments presented show the asymptotic values of trapping and storage efficiency factors with multiple cycles of drainage and imbibition under an ideal homogeneous scenario and a more realistic heterogeneous one. The trapping efficiency factor reduces from 65% after the first redistribution stage to 51.5% after the second redistribution stage in the homogeneous experiment, while it reduces from 100% to 64.3% from the first to the second redistribution stage in the heterogeneous experiment. The enhanced trapping efficiency in the heterogeneous case can be attributed to the local structural trapping, i.e., pocket trapping, which is caused by combined heterogeneity structure and capillary barrier effect. For the homogeneous case, all trapped NWP mass is due to combined residual saturation and hysteresis caused by cyclic drainage and imbibition. Given the large dimensions and total duration of the experiments, only one realization was performed for each scenario. However, to consider the natural uncertainty of sandbox experiments, we have performed stochastic numerical simulations using a continuum-based model in *Gonzalez-Nicolas et al*. [2016].

The observations of these large tank sandbox experiments allow to draw the following conclusions:

1. When performed in relatively homogeneous systems, subsequent NWP injections have the ability to enhance the reservoir space invaded by the plume, increasing residual NWP saturations by hysteresis caused by drainage/imbibition cycles. Under constrained injection pressure, the injection rate for the two injection events linearly increases with time following the same trend.
2. For the heterogeneous case, injected NWP accumulates in clusters of high-permeability sand facies to form pools of higher saturation trapped behind capillary barriers. Connecting these separate plume pools are low-permeability sand facies through which the buoyant plume has to migrate to achieve high storage and trapping efficiency.
3. The constant NWP injection pressure in the heterogeneous case results in fluctuations in the injection rate, reflecting the effect of permeability structure, the evolution of plume clusters, and NWP migration through low-permeability facies that connecting these pools. This observation is relevant to field situations where reservoir injectivity can show significant variations in time.
4. Layer-type heterogeneity exerts a major control on the migration and trapping of the plume, leading to longer displacement times to reach stable trapping conditions, dampened vertical migration, and immobilization of larger fraction of injected mass within coarser sand zones.

The outcomes presented in this study highlight the convenience of sandbox experiments for mimicking a realistic aquifer configuration and interplay of governing forces. As part of the continuing effort to improve numerical predictions of storage capacity and efficiency, these surrogate systems are instrumental to identify the relevant migration and trapping phenomena that need to be considered by mathematical models.

For instance, given their capillary-dominated flow regime, these experiments lend themselves to benchmark the performance of existing and new two-phase flow simulators.

Acknowledgments
Funding for this research is provided by the U.S. Department of Energy through the National Energy Technology Laboratory's CO_2 sequestration R&D Program under grant DE-FE0004630 and National Science Foundation award EAR-1045282 through the Hydrologic Sciences Program. Supporting information is included as four Figures in an supporting information file, one Excel spreadsheet containing data corresponding to Figures 4–10, and two Excel spreadsheets (one for each scenario) with saturation distributions for each time step; any additional data may be obtained from the corresponding author (email: luca.trevisan@gmail.com). The authors wish to thank three anonymous reviewers for their careful review of the manuscript and the suggestion of improvements. LT thanks Tip Meckel and Susan Hovorka for insightful discussions and acknowledges additional funding from the Bureau of Economic Geology.

References

Agartan, E., L. Trevisan, A. Cihan, J. Birkholzer, Q. Zhou, and T. H. Illangasekare (2015), Experimental study on effects of geologic heterogeneity in enhancing dissolution trapping of supercritical CO_2, *Water Resour. Res.*, *51*, 1635–1648, doi:10.1002/2014WR015778.

Barth, G. R., M. C. Hill, T. H. Illangasekare, and H. Rajaram (2001), Predictive modeling of flow and transport in a two-dimensional intermediate-scale, heterogeneous porous medium, *Water Resour. Res.*, *37*(10), 2503–2512.

Barth, G. R., T. H. Illangasekare, and H. Rajaram (2003), The effect of entrapped nonaqueous phase liquids on tracer transport in heterogeneous porous media: Laboratory experiments at the intermediate scale, *J. Contam. Hydrol.*, *67*(1–4), 247–268.

Behzadi, H., and V. Alvarado (2012), Upscaling of upward CO_2 migration in 2D system, *Adv. Water Resour.*, *46*, 46–54.

Bennion, D. B., and S. Bachu (2006), Dependence on temperature, pressure, and salinity of the IFT and relative permeability displacement characteristics of CO_2 injected in deep saline aquifers, in *2006 SPE Annual Technical Conference and Exhibition*, Soc. of Petrol. Eng., San Antonio, Tex.

Birkholzer, J. T., and Q. Zhou (2009), Basin-scale hydrogeologic impacts of CO_2 storage: Regulatory and capacity implications, *Int. J. Greenhouse Gas Control*, *3*(6), 745–756.

Bryant, S. L., S. Lakshminarasimhan, and G. A. Pope (2008), Buoyancy-dominated multiphase flow and its effect on geological sequestration of CO_2, *SPE J.*, *13*(4), 447–454.

Buscheck, T. A., Y. Sun, M. Chen, Y. Hao, T. J. Wolery, W. L. Bourcier, B. Court, M. A. Celia, S. J. Friedmann, and R. D. Aines (2012), Active CO_2 reservoir management for carbon storage: Analysis of operational strategies to relieve pressure buildup and improve injectivity, *Int. J. Greenhouse Gas Control*, *6*, 230–245.

Cameron, D. A., and L. J. Durlofsky (2012), Optimization of well placement, CO_2 injection rates, and brine cycling for geological carbon sequestration, *Int. J. Greenhouse Gas Control*, *10*, 100–112.

Cavanagh, A. J., and R. S. Haszeldine (2014), The Sleipner storage site: Capillary flow modeling of a layered CO_2 plume requires fractured shale barriers within the Utsira Formation, *Int. J. Greenhouse Gas Control*, *21*, 101–112.

Cihan, A., J. T. Birkholzer, and M. Bianchi (2015), Optimal well placement and brine extraction for pressure management during CO_2 sequestration, *Int. J. Greenhouse Gas Control*, *42*, 175–187.

Cihan, A., J. Birkholzer, L. Trevisan, A. Gonzalez-Nicolas Alvarez, and T. Illangasekare (2016), Investigation of representing hysteresis in macroscopic models of two-phase flow in porous media using intermediate scale experimental data, *Water Resour. Res.*, doi:10.1002/2016WR019449, in press.

Cinar, Y., A. Riaz, and H. A. Tchelepi (2009), Experimental Study of CO_2 Injection Into Saline Formations, *SPE J.*, *14*(4), 588–594.

Coats, K. H., and B. D. Smith (1964) Dead-end pore volume and dispersion in porous media, *SPE J.*, *4*(1), 73–84, doi:0.2118/647-PA.

Craig, F. F. (1993), *The Reservoir Engineering Aspects of Waterflooding*, 134 pp., Henry L. Doherty Mem. Fund of AIME, Richardson, Tex.

Deng, H. L., P. H. Stauffer, Z. X. Dai, Z. S. Jiao, and R. C. Surdam (2012), Simulation of industrial-scale CO_2 storage: Multi-scale heterogeneity and its impacts on storage capacity, injectivity and leakage, *Int. J. Greenhouse Gas Control*, *10*, 397–418.

Doughty, C., and K. Pruess (2004), Modeling supercritical carbon dioxide injection in heterogeneous porous media, *Vadose Zone J.*, *3*(3), 837–847.

Eichel, H., R. Helmig, I. Neuweiler, and O. A. Cirpka (2005), Upscaling of two-phase flow processes in porous media, in *Upscaling Multiphase Flow in Porous Media: From Pore to Core and Beyond*, edited by D. B. Das and S. M. Hassanizadeh, pp. 237–257, Springer, Netherlands.

England, W. A., A. S. Mackenzie, D. M. Mann, and T. M. Quigley (1987), The movement and entrapment of petroleum fluids in the subsurface, *J. Geol. Soc. London*, *144*, 327–347.

Fagerlund, F., T. H. Illangasekare, and A. Niemi (2007), Nonaqueous-phase liquid infiltration and immobilization in heterogeneous media: 1. Experimental methods and two-layered reference case, *Vadose Zone J.*, *6*(3), 471–482.

Farajzadeh, R., P. Ranganathan, P. L. J. Zitha, and J. Bruining (2011), The effect of heterogeneity on the character of density-driven natural convection of CO_2 overlying a brine layer, *Adv. Water Resour.*, *34*(3), 327–339.

Fernandez-Garcia, D., T. H. Illangasekare, and H. Rajaram (2004), Conservative and sorptive forced-gradient and uniform flow tracer tests in a three-dimensional laboratory test aquifer, *Water Resour. Res.*, *40*, W10103, doi:10.1029/2004WR003112.

Flett, M., R. Gurton, and I. Taggart (2004), The function of gas-water relative permeability hysteresis in the sequestration of carbon dioxide in saline formations, paper SPE 88485 presented at the SPE Asia Pacific Oil and Gas Conference and Exhibition, Perth, Australia, 18–20 Oct.

Flett, M., R. Gurton, and G. Weir (2007), Heterogeneous saline formations for carbon dioxide disposal: Impact of varying heterogeneity on containment and trapping, *J. Petrol. Sci. Eng.*, *57*(1–2), 106–118.

Frette, V., J. Feder, T. Jossang, and P. Meakin (1992), Buoyancy-driven fluid migration in porous-media, *Phys. Rev. Lett.*, *68*(21), 3164–3167.

Freyberg, D. L. (1986), A natural gradient experiment on solute transport in a sand aquifer. 2: Spatial moments and the advection and dispersion of nonreactive tracers, *Water Resour. Res.*, *22*(13), 2031–2046.

Gasda, S. E., M. A. Celia, and J. M. Nordbotten (2008), Upslope plume migration and implications for geological CO_2 sequestration in deep, saline aquifers, *IES J. Part A*, *1*(1), 2–16.

Gershenzon, N. I., R. W. Ritzi, D. F. Dominic, M. Soltanian, E. Mehnert, and R. T. Okwen (2015), Influence of small-scale fluvial architecture on CO_2 trapping processes in deep brine reservoirs, *Water Resour. Res.*, *51*, 8240–8256, doi:10.1002/2015WR017638.

Glass, R. J., S. H. Conrad, and W. Peplinski (2000), Gravity-destabilized nonwetting phase invasion in macroheterogeneous porous media: Experimental observations of invasion dynamics and scale analysis, *Water Resour. Res.*, *36*(11), 3121–3137.

Goater, A. L., B. Bijeljic, and M. J. Blunt (2013), Dipping open aquifers—The effect of top-surface topography and heterogeneity on CO_2 storage efficiency, *Int. J. Greenhouse Gas Control*, *17*, 318–331.

González-Nicolás, A., L. Trevisan, T. H. Illangasekare, A. Cihan, and J. T. Birkholzer (2016), Enhancing capillary trapping effectiveness through proper time scheduling of injection of supercritical CO_2 in heterogeneous formations, *Greenhouse Gas Sci Technol.*, in press.

Gunn, I., and A. W. Woods (2011), On the flow of buoyant fluid injected into a confined, inclined aquifer, *J. Fluid Mech.*, *672*, 109–129.

Han, W. S., S. Y. Lee, C. A. Lu, and B. J. McPherson (2010), Effects of permeability on CO_2 trapping mechanisms and buoyancy-driven CO_2 migration in saline formations, *Water Resour. Res.*, *46*, W07510, doi:10.1029/2009WR007850.

Hesse, M., H. A. Tchelepi, and F. M. Orr (2006), Scaling analysis of the migration of CO_2 in saline aquifers, paper presented at the SPE Annual Technical Conference and Exhibition, Soc. of Pet. Eng., San Antonio, Tex., 24–27 Sept.

Huber, E. J., A. D. Stroock, and D. L. Koch (2016), Analysis of a time dependent injection strategy to accelerate the residual trapping of sequestered CO_2 in the geologic subsurface, *Int. J. Greenhouse Gas Control*, *44*, 185–198.
Ide, S. T., K. Jessen, and F. M. Orr (2007), Storage of CO_2 in saline aquifers: Effects of gravity, viscous, and capillary forces on amount and timing of trapping, *Int. J. Greenhouse Gas Control*, *1*(4), 481–491.
Journel, A. G., and F. Alabert (1990), New method for reservoir mapping, *J. Petrol. Technol.*, *42*(2), 212–218.
Kopp, A., H. Class, and R. Helmig (2009), Investigations on CO_2 storage capacity in saline aquifers-Part 2: Estimation of storage capacity coefficients, *Int. J. Greenhouse Gas Control*, *3*(3), 277–287.
Kueper, B. H., and E. O. Frind (1991), Two-phase flow in heterogeneous porous media. 2: Model application, *Water Resour. Res.*, *27*(6), 1059–1070.
Kumar, A., M. Noh, G. A. Pope, K. Sepehrnoori, S. Bryant, and L. W. Lake (2005), Reservoir simulation of CO_2 storage in deep saline aquifers, *SPE J.*, *10*(3), 336–348.
Kuo, C. W., and S. M. Benson (2015), Numerical and analytical study of effects of small scale heterogeneity on CO_2/brine multiphase flow system in horizontal corefloods, *Adv. Water Resour.*, *79*, 1–17.
LaForce, T., J. Ennis-King, C. Boreham, and L. Paterson (2014), Residual CO_2 saturation estimate using noble gas tracers in a single-well field test: The CO2CRC Otway project, *Int. J. Greenhouse Gas Control*, *26*, 9–21.
Land, C. (1968), Calculation of imbibition relative permeability for two- and three-phase flow from rock properties, *SPE J.*, *8*(2), 149–156.
Larkin, R. (2010), Hydrodynamic trapping of CO_2 geosequestered in saline aquifers, paper presented at the SPE Improved Oil Recovery Symposium, Soc. of Pet. Eng., Tulsa, Okla., 24–28 April.
Lengler, U., M. De Lucia, and M. Kuhn (2010), The impact of heterogeneity on the distribution of CO_2: Numerical simulation of CO_2 storage at Ketzin, *Int. J. Greenhouse Gas Control*, *4*(6), 1016–1025.
Li, B. X., and S. M. Benson (2015), Influence of small-scale heterogeneity on upward CO_2 plume migration in storage aquifers, *Adv Water Resour.*, *83*, 389–404.
MacMinn, C. W., M. L. Szulczewski, and R. Juanes (2010), CO_2 migration in saline aquifers. Part 1: Capillary trapping under slope and groundwater flow, *J. Fluid Mech.*, *662*, 329–351.
Meckel, T. A., S. L. Bryant, and P. R. Ganesh (2015), Characterization and prediction of CO_2 saturation resulting from modeling buoyant fluid migration in 2D heterogeneous geologic fabrics, *Int. J. Greenhouse Gas Control*, *34*, 85–96.
Mikes, D., and J. Bruining (2006), Standard flow cells to incorporate small-scale heterogeneity (crossbedding) in a reservoir model, *Mar. Petrol. Geol.*, *23*(9–10), 979–993.
Myers, M., L. Stalker, T. La Force, B. Pejcic, C. Dyt, K.-B. Ho, and J. Ennis-King (2015), Field measurement of residual carbon dioxide saturation using reactive ester tracers, *Chem. Geol.*, *399*, 20–29.
Neufeld, J. A., M. A. Hesse, A. Riaz, M. A. Hallworth, H. A. Tchelepi, and H. E. Huppert (2010), Convective dissolution of carbon dioxide in saline aquifers, *Geophys. Res. Lett.*, *37*, L22404, doi:10.1029/2010GL044728.
Nordbotten, J. M., M. A. Celia, and S. Bachu (2005), Injection and storage of CO_2 in deep saline aquifers: Analytical solution for CO_2 plume evolution during injection, *Transp. Porous Media*, *58*(3), 339–360.
Pickup, G., P. S. Ringrose, and A. Sharif (2000), Steady-state upscaling: From lamina-scale to full-field model, *SPE J.*, *5*(2), 208–217.
Pini, R., S. C. Krevor, and S. M. Benson (2012), Capillary pressure and heterogeneity for the CO_2/water system in sandstone rocks at reservoir conditions, *Adv. Water Resour.*, *38*, 48–59.
Polak, S., Y. Cinar, T. Holt, and O. Torsaeter (2015), Use of low- and high-IFT fluid systems in experimental and numerical modelling of systems that mimic CO_2 storage in deep saline formations, *J. Petrol. Sci. Eng.*, *129*, 97–109.
Rasmusson, K., M. Rasmusson, F. Fagerlund, J. Bensabat, Y. Tsang, and A. Niemi (2014), Analysis of alternative push-pull-test-designs for determining in situ residual trapping of carbon dioxide, *Int. J. Greenhouse Gas Control*, *27*, 155–168.
Rasmusson, K., M. Rasmusson, Y. Tsang, and A. Niemi (2016), A simulation study of the effect of trapping model, geological heterogeneity and injection strategies on CO_2 trapping, *Int. J. Greenhouse Gas Control*, *52*, 52–72.
Remy, N., A. Boucher, and J. Wu (2009), *Applied Geostatistics With SGeMS: A User's Guide*, xix, 264 pp., Cambridge Univ. Press, Cambridge, UK.
Ringrose, P. S., K. S. Sorbie, P. W. M. Corbett, and J. L. Jensen (1993), Immiscible flow behaviour in laminated and cross-bedded sandstones, *J. Petrol. Sci. Eng.*, *9*(2), 103–124.
Ritzi, R. W., J. T. Freiburg, and N. D. Webb (2016), Understanding the (co) variance in petrophysical properties of CO_2 reservoirs comprising sedimentary architecture, *Int. J. Greenhouse Gas Control*, *51*, 423–434.
Saadatpoor, E., S. L. Bryant, and K. Sepehrnoori (2010), New Trapping mechanism in carbon sequestration, *Transp. Porous Media*, *82*(1), 3–17.
Sakaki, T., and T. H. Illangasekare (2007), Comparison of height-averaged and point-measured capillary pressure-saturation relations for sands using a modified Tempe cell, *Water Resour Res*, *43*, W12502, doi:10.1029/2006WR005814.
Shamshiri, H., and B. Jafarpour (2012), Controlled CO_2 injection into heterogeneous geologic formations for improved solubility and residual trapping, *Water Resour. Res.*, *48*, W02530, doi:10.1029/2011WR010455.
Singh, V., A. Cavanagh, H. Hansen, B. Nazarian, M. Iding, and P. Ringrose (2010), Reservoir modeling of CO_2 plume behavior calibrated against monitoring data from Sleipner, Norway, paper presented at the SPE Annual Technical Conference and Exhibition, Soc. of Pet. Eng., Florence, Italy, 19–22 Sept.
Tchelepi, H. A., and F. M. Orr (1994), Interaction of viscous fingering, permeability heterogeneity, and gravity segregation in three dimensions, *SPE Reservoir Eng.*, *9*(04), 266–271.
Tian, L., Z. Yang, F. Fagerlund, and A. Niemi (2016), Effects of permeability heterogeneity on CO_2 injectivity and storage efficiency coefficient, *Greenhouse Gases*, *6*(1), 112–124.
Trevisan, L. (2015), Study of trapping mechanisms of supercritical carbon dioxide in deep heterogeneous geological formations through intermediate-scale testing and modeling, PhD thesis, 189 pp, Colorado Sch. of Mines, Golden, Colo.
Trevisan, L., A. Cihan, F. Fagerlund, E. Agartan, H. Mori, J. T. Birkholzer, Q. Zhou, and T. H. Illangasekare (2014), Investigation of mechanisms of supercritical CO_2 trapping in deep saline reservoirs using surrogate fluids at ambient laboratory conditions, *Int. J. Greenhouse Gas Control*, *29*, 35–49.
Trevisan, L., R. Pini, A. Cihan, J. T. Birkholzer, Q. Zhou, and T. H. Illangasekare (2015), Experimental analysis of spatial correlation effects on capillary trapping of supercritical CO_2 at the intermediate laboratory scale in heterogeneous porous media, *Water Resour. Res.*, *51*, 8791–8805, doi:10.1002/2015WR017440.
Trevisan, L., P. G. Krishnamurthy, and T. A. Meckel (2017), Impact of 3D capillary heterogeneity and bedform architecture at the sub-meter scale on CO_2 saturation for buoyant flow in clastic aquifers, *Int. J. Greenhouse Gas Control*, *56*, 237–249.

van Lingen, P. P., J. Bruining, and C. P. J. W. van Kruijsdijk (1996), Capillary entrapment caused by small-scale wettability heterogeneities, *SPE Reservoir Eng.*, *11*(2), 93–100.

Werner, M., D. Sutter, A. Krattli, O. Lafci, R. Mutschler, P. Oehler, J. Winkler, and M. Mazzotti (2014), A physical model for geological CO_2 storage—Replacing misconceptions by visual explanation, *Int. J. Greenhouse Gas Control*, *25*, 42–53.

Yamamoto, H., K. Zhang, K. Karasaki, A. Marui, H. Uehara, and N. Nishikawa (2009), Numerical investigation concerning the impact of CO_2 geologic storage on regional groundwater flow, *Int. J. Greenhouse Gas Control*, *3*(5), 586–599.

Zhao, B. Z., C. W. MacMinn, H. E. Huppert, and R. Juanes (2014), Capillary pinning and blunting of immiscible gravity currents in porous media, *Water Resour. Res.*, *50*(9), 7067–7081, doi:10.1002/2014WR015335.

Zhou, Q., J. T. Birkholzer, E. Mehnert, Y.-F. Lin, and K. Zhang (2010), Modeling basin- and plume-scale processes of CO_2 storage for full-scale deployment, *Ground Water*, *48*(4), 494–514.

Zimoch, P. J., J. A. Neufeld, and D. Vella (2011), Leakage from inclined porous reservoirs, *J. Fluid Mech.*, *673*, 395–405.